Algorithmic scatter correction in dual-energy digital mammography for calcification imaging

Xi Chen [a], Robert M. Nishikawa[b], Suk-tak Chan[c], Beverly A. Lau[b], Lei Zhang[d], Xuanqin Mou*[a]

[a]Institute of Image Processing & Pattern Recognition, Xi'an Jiaotong University, Xi'an, Shaanxi, 710049, China;

[b]Department of Radiology, The University of Chicago, Chicago, Illinois 60637;

[c]Department of Health Technology and Informatics, The Hong Kong Polytechnic University, Hung Hom, Hong Kong

[d]Department of Computing, The Hong Kong Polytechnic University, Hung Hom, Hong Kong

ABSTRACT

X-ray scatter leads to erroneous calculations of dual-energy digital mammography (DEDM). The purpose of this work is to design an algorithmic method for scatter correction in DEDM without extra exposures or lead sheet. The method was developed based on the knowledge that scatter radiation in mammograms varies slowly spatially and most pixels in mammograms are non-calcification pixels, and implemented on a commercial full-field digital mammography system with a phantom of breast tissue equivalent material. The pinhole-array interpolation scatter correction method was also implemented on the system. We compared the background dual-energy (DE) calcification signals in the DE calcification images. Results show that the background signal in the DE calcification image can be reduced. The rms of background DE calcification image signal of 1105μm with scatter-uncorrected data was reduced to 187μm and 253μm after scatter correction, using our algorithmic method and pinhole-array interpolation method, respectively. The range of background DE calcification signals using scatter-uncorrected data was reduced by ~80% with scatter-corrected data using algorithmic method. The proposed algorithmic scatter correction method is effective; it has similar or even better performance than pinhole-array interpolation method in scatter correction for DEDM.

Keywords: dual-energy, digital mammography, scatter correction, calcification

1. INTRODUCTION

Microcalcifications are often the earliest and the main indicator of breast cancer[1]. Calcifications have greater x-ray attenuation coefficients than the surrounding breast tissues, so they are more visible on homogeneous soft-tissue backgrounds. However, the visualization of calcifications could be obscured in mammograms because of overlapping of tissue structures. Tissue structures in mammograms arise from the differences of the x-ray attenuation coefficients between adipose tissue, glandular tissue, ducts, vessels, soft-tissue masses. Dual-energy digital mammography (DEDM) has been considered as a promising technique to improve the detectability of calcifications since it can be used to suppress the contrast between adipose and glandular tissues of the breast[2-6].

One important concern for DEDM imaging is the scattered radiations arising from the x-ray beam. In the experiment of Cooper III et al.[7], the measured Scatter-to-Primary Ratios (SPRs) at 28kVp for 4-cm-thick breast phantom were 0.3960 for 0% glandular, 0.3560 for 43% glandular and 0.4260 for 100% glandular, respectively. In clinical full-field digital mammography system, anti-scatter grids are usually used during image acquisition, although effective in the suppression of scatter, do not completely eliminate the scatter. Scattered radiation can still traverse the grid. In Kappadath and Shaw's experiment[4], scatter fractions range from 17% to 22% and from 20% to 25% in the LE and HE wedge phantom images with grid using the full-field digital mammography system (Senographe 2000D, GE Medical Systems, Milwaukee, WI, USA). Scattered radiation contributes mainly to noise increase and contrast degradation in single energy image. DE imaging will suffer further degeneration, like the serious deterioration of the signal of interest.

*xqmou@mail.xjtu.edu.cn; phone 86 29 82663719; ipl.xjtu.edu.cn

Kappadath and Shaw[4] adopted pinhole-array interpolation method for scatter correction in DEDM. This method employed a lead sheet containing an array of pinholes to acquire spot measurements of the primary radiations, and then the scattered radiation at the spot locations can be obtained. The scatter signal in the entire full-field image was estimated by fitting a smooth surface to the scatter at the spot locations. This technique needs extra exposures, complicates the manipulation and is impractical for DEDM in clinic. Other methods to reduce scattered radiations, such as applying an air gap[8], employing a slot scanning system[9-10] or multi-slit scanning system[11], require a completely new system design for mammography unit.

We proposed a scatter correction algorithm which exploits the characteristic that scatter in mammograms is a quantity of low-frequency and the fact that most pixels in mammograms are non-calcification pixels. It is convenient and there is no extra exposures. We presented the performance of this algorithmic scatter correction method by breast phantom studies implemented on a commercial full-field digital mammography system. We also implemented the pinhole-array interpolation scatter correction method on the system for comparison. Phantom results for both methods are presented and discussed. The total entrance-skin exposure and mean glandular dose used for the LE and HE images were constrained to be similar to screening examination levels.

2. THEORY

2.1 Dual-energy digital mammography calculation

Lemacks et al.[2] proposed a numerical framework to perform the DEDM calculation. They assumed that there are three attenuating materials in the breast: adipose tissue (thickness t_a), glandular tissue (thickness t_g), and calcification (thickness t_c). Depending on the distribution of materials, the transmitted fluence incident on the detector is given by

$$P(E) = P_0(E)\exp\left[-\mu_a(E)t_a - \mu_g(E)t_g - \mu_c(E)t_c\right],$$
(1)

where $P_0(E)$ and $P(E)$ are the incident photon fluence on the surface of the breast and the transmitted fluence, respectively; and $\mu_a(E)$, $\mu_g(E)$ and $\mu_c(E)$ are linear attenuation coefficients of adipose tissue, glandular tissue and calcification, respectively. However, only two unknowns can be solved in DEDM. In a mammographic examination, breast is usually compressed to a uniform thickness T that is automatically measured by the x-ray system. The contribution of calcifications to the total breast thickness can be ignored because the calcifications are small in size and sparsely present i.e. $T \approx t_a + t_g$. With the total breast thickness T known, the three unknowns t_a, t_g and t_c can be expressed as two unknowns: glandular ratio $g = t_g / T \approx t_g / (t_a + t_g)$ and calcification thickness t_c. Now, Eq. (1) can be rewritten as

$$P(E) = P_0(E)\exp\left[-\mu_a(E)T - g\left(\mu_g(E) - \mu_a(E)\right)T - \mu_c(E)t_c\right].$$
(2)

In DE imaging calculations, a reference signal I_r is needed to change the dynamic range of the intensity values. The exposure data f is defined as the logarithmic value of the ratio of transmitted signal I to reference signal I_r. The HE and LE logarithmic intensities $f_l(t_c, g)$ and $f_h(t_c, g)$ are measured independently using x-ray beams at different kVps:

$$f_j(t_c, g) = \ln\left(I_{rj}/I_j\right)$$
$$= \ln\left(I_{rj}\right) - \ln\left(\int P_{0j}(E)\exp\left[-\mu_a(E)T - g\left(\mu_g(E) - \mu_a(E)\right)T - \mu_c(E)t_c\right]Q(E)dE\right),$$
$$j = l, h. \quad (3)$$

where $Q(E)$ is the detector response.

In medical diagnostic x-ray imaging modalities, poly-energetic spectra are often used which results in a nonlinear relationship between (f_l, f_h) and (t_c, g). In this paper, an inverse-map function

$$t_c = \frac{a_0 + a_1 f_l + a_2 f_h + a_3 f_l^2 + a_4 f_l f_h + a_5 f_h^2 + a_6 f_l^3 + a_7 f_l^2 f_h + a_8 f_l f_h^2 + a_9 f_h^3}{b_0 + b_1 f_l + b_2 f_h + b_3 f_l^2 + b_4 f_l f_h + b_5 f_h^2}$$
(4)

was used to describe the relationship between calcification thickness t_c and (f_l, f_h). The coefficients a_k $(k=0,...,9)$ and b_k $(k=0,...,5)$ were determined by a least-squares fit of the calibration data.

2.2 Scatter representation

The signal measured in each pixel of the detector is the sum of the signal from the primary radiation, P, and that from scattered radiation, S. For any pixel in the LE or HE images, let:

$$I_j' = P_j + S_j, \quad j = l, h$$

(5)

where P_j is the primary radiation, S_j is the scattered radiation, and I_j' is the measured signal. Then, f_j $(j=l,h)$ can be rewritten as

$$f_j = \ln(I_{rj}/(I_j' - S_j)), \quad j = l, h$$

(6)

Substituting Eq.(6) into Eq.(4), we would like to solve for the scatter S_l and S_h. It can be seen that the coefficients a_k and b_k, reference signals I_{rl} and I_{rh}, measured signals I_l' and I_h' are all known values, and three unknowns t_c, S_l and S_h need to be solved. It is impossible to solve three unknowns using one equation. However, scatter in mammograms is a quantity of low-frequency because the breast is usually compressed to a largely uniform thickness during mammography. Therefore, the scatter of one pixel can be represented by the scatter of its neighbor pixels, just as shown in Figure 1, linear interpolation used, scattered radiation of pixel B1 can be represented as

$$S_{B1j} = (S_{A1j} + S_{A2j})/2, \quad j = l, h$$

(7)

and scattered radiation of pixel C1 can be represented as

$$S_{C1j} = (S_{A1j} + S_{A2j} + S_{A5j} + S_{A6j})/4, \quad j = l, h$$
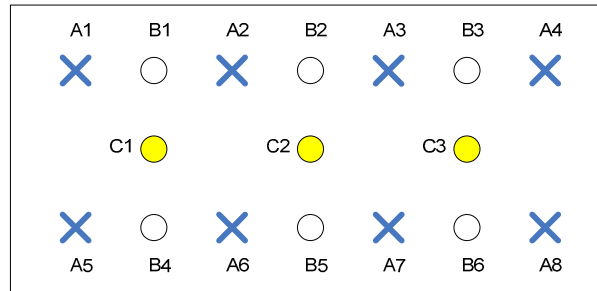
(8)

Figure 1 Schematic of the pixel location.

2.3 Scatter estimation

For an imaged object, both LE and HE images are acquired. We sample N pixels in LE image and N corresponding pixels in HE image, respectively. These N pixel pairs can be put into two categories: independent pixel pairs and dependent pixel pairs. k_1 pairs belong to independent pixel pairs whose scatter are unknowns, such as pixels Ai $(i=1,..,8)$ in Figure 1; k_2 $(k_2 > k_1)$ pairs are dependent pixel pairs whose scatter are represented by those of independent pairs, such as pixels Bi$(i=1,..,6)$, C1, C2 and C3.

Since most pixels in mammograms are non-calcification pixels, the sampled pixels can be considered as non-calcification pixels, thereby their corresponding t_c is zero. Then, we can set up an equation set with N equations [Each one is Eq.(4).]. In this equation set, there are $2k_1$ unknowns S_{ij} $(i=1,..., k_1; j=l, h)$ to be determined. Since $N = k_1 + k_2 > 2k_1$, the $2k_1$ unknowns S_{ij} can be determined by a least-squares estimate of the measured signals I_{ij}' ($i=1,...,N; j=l, h$) of the N pixel pairs. So the scattered radiations S_{ij} of the k_1 pixel pairs can be determined, scatter radiations of other pixels can be obtained by interpolation. And then, a pixel by pixel estimate of the scatter fields for the LE and HE image can be generated.

3. MATERIALS AND METHODS

3.1 Dual-energy imaging techniques

The mammography system used in this study was a full-field digital mammography system (Senographe Essential, GE Medical Systems, Milwaukee, WI, USA). The detector consisted of a CsI:Tl converter layer coupled with an aSi:H+TFT flat-panel detector. The image size was 3062×2394 with a pixel size of 100μm. For-processing ("raw") images were used for our DE calculations. The imaging conditions selected in this study were similar to those in the previous studies[3-4], the total mean-glandular dose and entrance-skin exposure were constrained to typical screening examination levels: 28kVp at 50mAs for LE imaging and 48kVp at 12.5mAs for HE imaging. There were four focal spots in the system: 100μm and 300μm on Mo target, 100μm and 300μm on Rh target. We standardized the focal spot size to 300μm on the Rh target with Rh filter for LE and HE imaging in this experiment because of the limited hardware option for 48kVp in HE imaging and the possible misregistration if two different focal spots were used for LE and HE imaging. The source to image distance was 66cm and the compression plate was removed during image acquisition. The anti-scatter grid was used during image acquisition.

3.2 Phantom for imaging

For this study, a physical breast phantom (Model 017, Computerized Imaging Reference Systems Inc., Norfolk, VA, USA) was used as the imaged object (Figure 2). The phantom was a rectangular block with dimension of $12×10×4cm^3$ (length×width×height). This model was a density step phantom that simulated different ratios of glandular and adipose tissues. The materials of this phantom mimicked the photon attenuation coefficients of a range of breast tissues. The average elemental composition of the human breast being mimicked was based on the individual elemental composition of adipose and glandular tissues reported by Hammerstein et al.[12]. The glandular ratio ranged from 0% to 100% in six steps, 0%, 30%, 45%, 50%, 70% and 100%. There was water equivalent bolus on each end. The inner clear acrylic section was not included in our calculation and comparison, since acrylic is not a stable representation of breast tissue across a wide x-ray energy range.
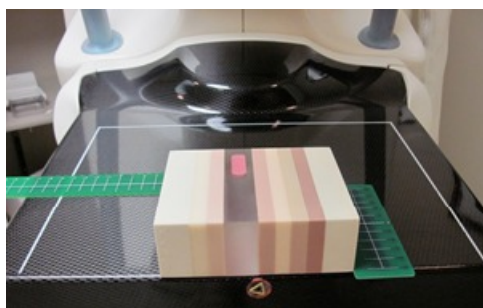

Figure 2 Breast phantom CIRS Model 017.

3.3 Calibration procedure

When we use different materials for calibration measurement and imaging, the attenuation differences between imaged object and calibration phantoms can bring large calculation errors[5]. In order to investigate the scatter correction method independently, we used the same breast phantom for both calibration measurement and imaging. A mammographic aluminum stepwedge (Model 118, GAMMEX Inc., Middleton, WI, USA) was used to simulate calcifications for calibration measurement. The wedge was 1.5cm wide, 11.5cm long and had 9 steps, each 250μm high; the copper backing strip and the plastic coat were removed during measurement. The calibration measurement was performed at five glandular ratios (0%, 30%, 50%, 70%, and 100%) of the 4-cm-thick breast phantom and at five aluminum thicknesses (0, 250, 500, 750, 1000μm). Since the glandular ratio 45% is close to 50% and five glandular ratios were fairly enough for calibration, 45% glandular ratio of CIRS Model 017 was not used in calibration. In order to reduce the statistical uncertainties of the calibration measurements, the mAs were increased. The x-ray spectra used were 28kVp at 100mAs and 48kVp at 16mAs for LE and HE calibration measurement, respectively, both with Rh anode and Rh filter. Additionally, we measured the uncertainties of the signals of 50, 100, 200 and 320mAs at 28kVp; and 12.5, 16, 18 and 22.5mAs at 48kVp. The results indicated that the uncertainties had no obvious decrease when mAs were increased higher than 100mAs at 28kVp and 16mAs at 48kVp in our digital mammography system. In order to avoid the high tube loading, we used 100mAs at 28kVp and 16mAs at 48kVp in calibration measurement.

The calibration measurement was carried out under narrow-beam geometry as shown in Figure 3. The x-ray beam was defined by a pre-collimator on the tube side of the phantom and by a post-collimator on the breast support. Each collimator was a 1-mm-thick lead sheet with a 5mm diameter hole. The two collimators were carefully aligned. The average value of the central 11×11 pixels in the collimator area was used as calibration data. We have verified by Monte Carlo simulation[13-14] that a very small amount of scatter (1.6% for LE images and 1.5% for HE images) was present in the central 11×11 pixels. The coefficients of Eq.(4) were estimated using a non-linear least-squares fitting to the calibration data. The median, maximum and rms of the fitting errors were 0.1, 71 and 29μm, respectively.
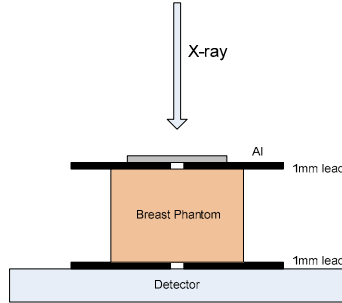

Figure 3 Schematic of the calibration measurements under narrow-beam geometry.

3.4 Pinhole-array interpolation method

To verify the scatter correction method proposed in this study, the primary and scattered radiations were experimentally determined by pinhole-array interpolation method. With this method, a 3-mm-thick lead sheet with pinhole-array was placed underneath the breast phantom for imaging. The lead sheet consisted of a 2D array of pinholes, 1mm in diameter and spaced center to center 1 cm vertically and horizontally. In the LE and HE phantom images acquired with the lead sheet in place, the radiations in the aperture areas were mostly primary signals. The signals outside the aperture were almost zero. The LE and HE phantom images acquired without the lead sheet in place contained both the primary and scattered radiations. In practice, when acquiring images without lead sheet, a 3-mm-thick acrylic sheet with a 11.7×9.7cm^2 rectangular hole replaced the lead sheet. Thereby, a 3mm air-gap was between the phantom and the breast support and the distance from the phantom to the focal spot was fixed with or without the lead sheet. The images acquired with the lead sheet may be subtracted from those acquired without the lead sheet to estimate the scatter component in the aperture areas. For each pinhole, signals in a 2×2 pixels region at the center were averaged and used to estimate the primary signal $P(x, y)$, and the primary plus scatter signal $I(x, y)$, at the aperture center (x, y). Thus, the scatter component $S(x, y)$ may be estimated by subtracting the two signals: $S(x, y) = I(x, y)-P(x, y)$. Scatter radiations of other pixels (not in pinhole) can be obtained by interpolation.

4. RESULTS

Scatter fraction were estimated using the proposed algorithmic method and pin-hole array interpolation method and three DE calcification images: image with scatter correction using our algorithmic method, image with scatter correction using pinhole-array interpolation method, and image without scatter correction, were compared in this part.

First, the LE and HE images of the breast phantom were acquired. Next, the LE and HE images of the breast phantom with the pinhole-array lead sheet were acquired. And then, we constructed the LE and HE reference images. A 4-cm-thick Lucite phantom was exposed at 28kVp (5 times) and 48kVp (5 times). The reference LE or HE image generated was an average of the five images separately acquired to minimize the random noise fluctuations. Additionally, the reference image was filtered by a low-pass filter (boxcar) with the kernel size of 31×31 pixels to further reduce the noise. When computing $f_j=ln(I_{rj}/I_j)$ $(j=l,h)$ of each pixel in the LE or HE phantom image, we used the pixel values on the corresponding locations in the reference image as the reference signal I_{rj}.

Since the phantom imaged had physical dimensions of 12×10×4 cm^3 with 2×10×4 cm^3 water equivalent bolus on each end, the acquired images were trimmed and only 1000×800 pixels were kept (Figure 4). We sampled 150 (N=150) pixels in the LE phantom image and the corresponding 150 pixels in the HE image, including 60 (k_1 =60, red asterisks)
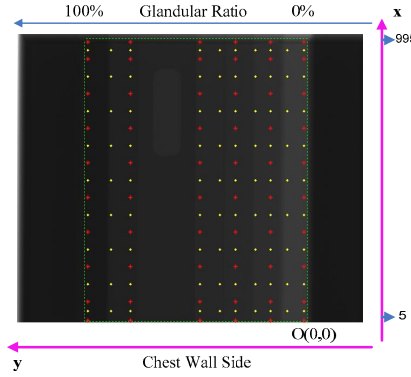
Figure 4 High energy image of breast phantom, the region inside the green dashed lines is 1000×800 pixels, red asterisks indicate independent pixels and yellow dots indicate dependent pixels in algorithmic scatter correction method.

independent pixel pairs and 90 (k_2=90, yellow dots) dependent pixel pairs. We did not sample pixels in the acrylic area. Independent pixel pairs were sampled from x=5 pixel to x=995 pixel, and hence, 12 independent pixel pairs located along the edge of the phantom. Smaller sampling interval was used near the edge of the phantom where the scatter profiles change relatively faster. The sampling interval was around 60 pixels close to the edge. The other sampling interval was about 120 pixels. Pixel values of the same locations in the reference images were selected. Therefore, we constructed an equation set with 150 equations [Each one was Eq. (4) and t_c was forced to zero.] and 120 unknowns S_{ij} ($i=1,..., 60;j=l, h$). A least-squares algorithm was employed to estimate S_{ij}. Using these S_{ij} of the sampled pixels we generated an estimate of scatter field by cubic interpolating and then subtracting it from the phantom image.

4.1 Scatter fraction estimation

We applied the proposed algorithmic method and pinhole-array interpolation method to generate the scatter fields of the LE and HE images. The SPR (S_{ij}/P_{ij}) measured by the pinhole-array interpolation method and the proposed algorithmic method at the same locations are listed in Table I. The surface plots of the scatter signal estimated using this algorithmic method and pinhole-array interpolation method for LE and HE images are shown in Figure 5. The shapes of the scatter field estimated using the two different methods looked the same. The error of scatter estimate was higher when glandular ratio was increased to 100%. Overall, the proposed scatter estimation method worked well, especially for the HE image.

4.2 DE calcification image evaluation

Ideally, the DE calcification image signal t_c would fluctuate around zero since there was no calcification in the phantom. Such calcification image signal was referred to as background DE calcification image signal. As shown in Table II~IV, we compared the t_c values of some selected pixels in the three background DE calcification image.

There are 60 background calcification signals t_c presented in Table II, which came from the calcification image calculated based on the pinhole-array interpolation scatter correction. These corresponding 60 pixel pairs lay at the locations of the center of pinholes. We also adopted these pixels pairs as independent pairs and estimated their scatter signal S_{ij} ($i=1,..., 60;j=l, h$) using our algorithmic method. The resultant background calcification signals t_c are listed in Table III. The background calcification signals t_c calculated without scatter correction are listed in Table IV. The background DE calcification signals calculated based on the pinhole-array interpolation scatter correction method (Table II) were somewhat nonuniform (median ~12μm, rms ~277μm and range ~1420μm). The calcification thickness calculated based on the algorithmic scatter correction method (Table III) yielded approximately a uniform distribution (median ~0μm, rms ~66μm and range ~411μm) of background signals. In contrast, the calcification thickness computed without scatter correction (Table IV) yielded a structured nonuniform distribution (median ~1028μm, rms ~577μm and range ~2344μm) of background signals which varied somewhat along the direction of varying glandular ratio.

Table I SPR measured by algorithmic method and pinhole-array interpolation method on the same locations of different glandular ratios in breast phantom.

Image	Method	Glandular ratio (%)					
		0	30	45	50	70	100
LE	algorithmic	12.1	13.1	15.0	15.2	16.1	17.0
	pinhole	12.3	12.9	12.1	13.1	11.6	13.6
HE	algorithmic	15.9	17.0	16.2	16.6	16.9	17.6
	pinhole	16.0	16.9	15.8	14.2	14.7	16.5

(a)   (b)

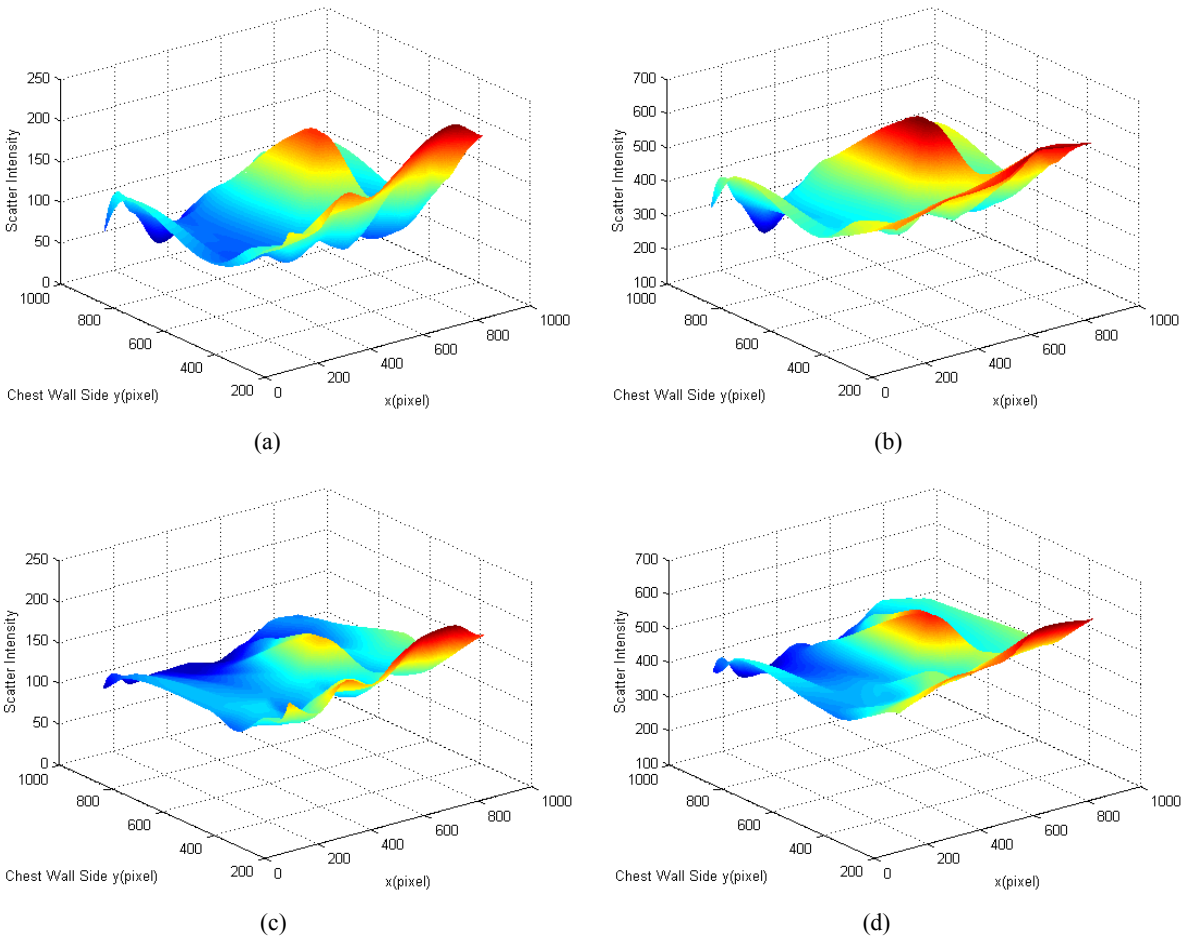
(c)   (d)

Figure 5 Scatter signal field estimated using the algorithmic method and pinhole-array interpolation method: (a) algorithmic method LE, (b) algorithmic method HE, (c) pinhole-array interpolation method LE, (b) pinhole-array interpolation method HE.

However, the individual pixel values were susceptible to noise fluctuations, so the median and rms values in 35 regions-of-interest (ROI) of size 31×31 pixels across the image were computed to estimate the background calcification signal and noise fluctuations. ROIs were selected in the regions of glandular ratios 0%, 30%, 45%, 50% and 70%. In Table V, the median, minimum, and maximum background DE calcification signals in the 5×7 array of ROI, using scatter corrected and uncorrected images, are listed for comparison. The median background signals for the three DE calcification images are also plotted for comparison in Figure 6.

We observed reduced DE background signal after scatter correction, both scatter correction techniques were effective. However, the reduction was more pronounced using the algorithmic method rather than the pinhole-array interpolation method for scatter correction. The rms of background DE calcification image signal of 1105μm with scatter-uncorrected data was reduced to 187μm and 253μm after scatter correction, using our algorithmic method and pinhole-array interpolation method, respectively. According to the minimum and maximum values of ROI signal listed in Table V, the

range of background DE calcification signals can be estimated. The range of background DE calcification signals using scatter-uncorrected data was reduced by ~80% and by ~52% with scatter-corrected data by algorithmic method and pinhole-array interpolation method, respectively.

Table II Background calcification signals calculated based on the pinhole-array interpolation scatter correction, the 60 pixel pairs lay on the locations of the center of pinholes.

Glandular ratio (%)	Background calcification signal t_c (μm)									
0	-54	13	-13	-27	-45	-40	-125	-177	-131	-161
30	129	193	29	107	119	-77	-106	-216	727	-221
45	301	294	331	117	55	26	-221	133	-127	-183
50	484	271	242	151	230	-164	106	121	140	-274
70	290	64	79	553	12	278	-132	-74	-44	-324
100	-216	141	106	117	-683	-401	-483	-584	-564	-693

Table III Background calcification signals calculated based on algorithmic scatter correction, the pixel pairs were independent pairs in algorithmic method.

Glandular ratio (%)	Background calcification signal t_c (μm)									
0	-29	-23	-9	13	-4	-16	-22	37	-82	-112
30	-28	-26	25	14	0	4	-19	-64	-13	-4
45	10	32	14	42	2	-10	-139	82	-137	-135
50	2	25	30	33	55	-82	55	67	86	-118
70	-71	-65	-37	272	78	3	28	25	70	45
100	-22	-35	-10	9	6	-62	-125	-45	1	-1

Table IV Background calcification signals without scatter correction, pixel pairs were the same as in Table II and III.

Glandular ratio (%)	Background calcification signal t_c (μm)									
0	2213	2494	2119	2300	2159	2650	2536	2814	2249	2900
30	1323	1310	1296	1292	1313	1301	1314	1291	1321	1529
45	1165	1105	1085	1083	1136	1074	1077	1147	1013	1020
50	1036	963	968	947	949	1070	923	899	944	850
70	820	926	657	938	983	937	882	847	895	766
100	881	983	824	834	955	839	855	747	822	566

Table V The median, minimum, and maximum background dual-energy calcification signals (μm) in the regions-of-interest with and without scatter correction.

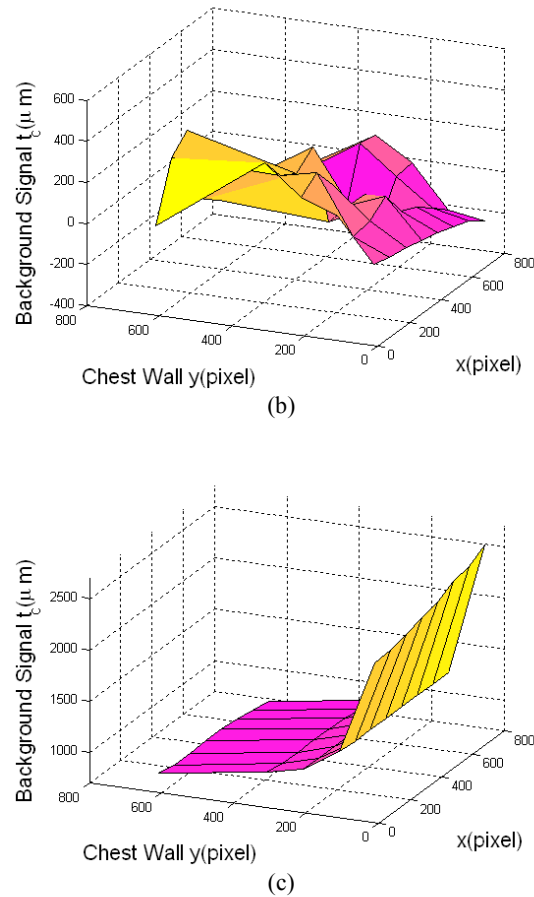| DE calcification image	ROI signal (μm)			ROI rms (μm)		
	Median	Min	Max	Median	Min	Max
Scatter correction algorithmic	-14	-189	129	187	37	809
Scatter correction pinhole	22	-282	446	253	38	944
Without scatter correction	1044	703	2219	1105	812	2945

(a)

(b)

(c)
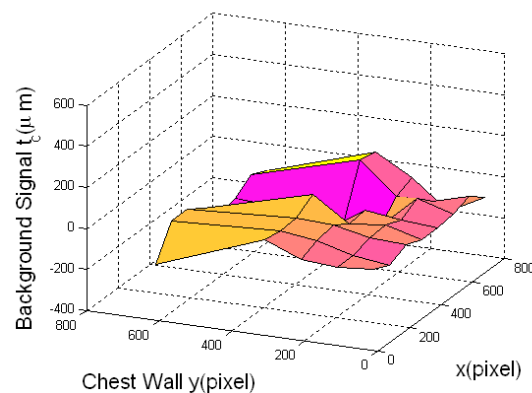
Figure 6 Median background signal in the 5×7 array of regions-of-interest of the three background dual-energy calcification images:
(a) scatter correction using our algorithmic method; (b) scatter correction using pinhole-array interpolation method; (c) without scatter correction.

5. CONCLUSION

The proposed algorithmic scatter correction is effective, when applying this scatter correction to images, the resultant background signal in the DE calcification image can be reduced. This method has similar or even better performance than pinhole-array interpolation method in scatter correction for DEDM. When applying the scatter correction to images, the resultant background signal in the DE calcification image can be reduced and the residual variation of background DE calcification signal was less than $\sim 200 \mu m$. Moreover, this method is convenient and there is no extra exposure to patient.

ACKNOWLEDGEMENTS

REFERENCES

[1] Fandos-Morera, A., Prats-Esteve, M., Tura-Soteras, JM. and Traveria-Cros, A., " Breast tumors: composition of microcalcifications," Radiology 169(2), 325-327 (1988).

[2] Lemacks, M., Kappadath, S., Shaw, C., Liu, X., Whitman, G., "A dual-energy subtraction technique for microcalcification imaging in digital mammography—A signal-to-noise analysis," Medical Physics 29(8), 1739-1751 (2002).

[3] Kappadath, S., Shaw C., "Quantitative evaluation of dual-energy digital mammography for calcification imaging," Physics in Medicine and Biology 49(10), 2563-2576 (2004).

[4] Kappadath, S., Shaw C., "Dual-energy digital mammography for calcification imaging: Scatter and nonuniformity corrections," Medical Physics 32 (11), 3395-3408 (2005).

[5] Mou, X., Chen, X., Sun, L., Yu, H., Ji, Z., Zhang, L., "The impact of calibration phantom errors on dual-energy digital mammography," Physics in Medicine and Biology 53(22), 6321-6336 (2008).

[6] Kappadath, S., Shaw C., "Dual-energy digital mammography for calcification imaging: noise reduction techniques," Physics in Medicine and Biology 53(19), 5421-5443 (2008).

[7] Cooper III, V. N., Boone, J. M., Seibert, J. A. and Pellot-Barakat, C. J., "An edge spread technique for measurement of the scatter-to-primary ratio in mammography," Medical Physics 27(5), 845-853 (2000).

[8] Krol, A., Bassano, D.A., Chamberlain C. C. and Prasad, S. C., "Scatter reduction in mammography with air gap," Medical Physics 23, 1263-1270 (1996).

[9] Jing, Z., Huda, W. and Walker, J. K. "Scattered radiation in scanning slot mammography," Medical Physics 25(7), 1111-1117 (1998).

[10] Liu, X., Shaw, C. C., Lai, C-J., Altunbas, M. C., Chen, L., Han, Y. and Wang, T., "Scatter rejection and low-contrast performance of a slot-scan digital chest radiography system with electronic aft-collimation: A chest phantom study," Medical Physics 35(6), 2391-2402 (2008).

[11] Barnes, G. T., Wu X. and Wagner, A. J. "Scanning slit mammography," Med. Prog. Technol.19 7-12 (1993).

[12] Hammerstein, G., Miller, D., White, D., Masterson, M., Woodard, H., Laughlin, J., "Absorbed radiation dose in mammography," Radiology 130(2), 485-491 (1979).

[13] Salvat, F., Fernández-Varea, J. M. and Sempau, J., "PENELOPE, A code System for Monte Carlo Simulation of Electron and Photon Transport," OECD Nuclear Energy Agency, Issy-les-Moulineaux, France, 2006.

[14] Sempau, J., Acosta, E., Baró, J., Fernáandez-Varea, J. M. and Salvat, F., "An algorithm for Monte Carlo simulation of coupled electron-photon transport," Nucl. Instrum. Meth. B 132, 377–390 (1997).